3D printed microneedle patches using stereolithography (SLA) for intradermal insulin delivery

AUTHOR NAMES

Sophia N. Economidou[1], Cristiane Patricia Pissinato Pere[1], Andrew Reid[2], Md. Jasim Uddin[3], James F.C. Windmill[2], Dimitrios A. Lamprou[4], Dennis Douroumis[1]**

AUTHOR ADDRESS

[1]Medway School of Pharmacy, University of Kent, Medway Campus, Central Avenue, Chatham Maritime, Chatham, Kent ME4 4TB, United Kingdom

[2]Centre for Ultrasonic Engineering, Department of Electronic and Electrical Engineering, University of Strathclyde, 204 George St, Glasgow, G1 1XW, Scotland, United Kingdom

[3]Department of Pharmacy, BRAC University, Bangladesh. Address: 41 Pacific Tower, Mohakhali, Dhaka-1212, Bangladesh.

[4] School of Pharmacy, Queen's University Belfast, 97 Lisburn Road, Belfast, BT9 7BL, United Kingdom

Keywords

3D printing, microneedles, inkjet coating, insulin, μCT

Abstract

3D printed microneedle arrays were fabricated using a biocompatible resin through stereolithography (SLA) for transdermal insulin delivery. Microneedles were built by polymerising consecutive layers of a photopolymer resin. Thin layers of insulin and sugar alcohol or disaccharide carriers were formed on the needle surface by inkjet printing. The optimization of the printing process resulted in superior skin penetration capacity of the 3D printed microneedles compared to metal arrays with minimum applied forces varying within the range of 2 to 5N. Micro–CT analysis showed strong adhesion of the coated films on the microneedle surface even after penetration to the skin. *In vivo* animal trials revealed fast insulin action with excellent hypoglycaemia control and lower glucose levels achieved within 60 min, combined with steady state plasma glucose over 4 h compared to subcutaneous injections.

Introduction

Transdermal Drug Delivery (TDD), the ability to effectively convey drugs through the human skin, is an appealing concept, aiming at surpassing the pitfalls of the traditional administration routes. The broader adoption of the transdermal route, however, is hampered by restrictions that stem from the nature of the skin barrier itself, especially by the stratum corneum. Microneedles (MNs) are small devices that can pierce this outermost, most impermeable layer of the human skin and successfully deliver active substances such as drugs, Ribonucleic acid (RNA), Deoxyribonucleic acid (DNA), and vaccines straight into the dermal microcirculation [1–4] . Due to their small size they leave skin nerves intact upon insertion [5], while they increase

bioavailability since the drug does not pass through any metabolic systems [6]. The MN-mediated drug delivery is realised through multiple strategies that employ solid, coated, hollow, hydrogel-forming and soluble MNs [7].

Since their introduction over 20 years ago, MN systems have attracted significant attention for their potential to replace traditional drug administration routes. In the field of diabetes type 1 and some types of type 2, the vast majority of patients rely on subcutaneous needle injections for insulin replacement, a treatment approach highly associated with reduced patient-compliance [8]. Pain, skin thickening due to recurring injections, needle phobia and insulin leakages on the skin surface [9,10] have motivated vigorous research on MN-based systems for transdermal insulin delivery.

Recent advances encompass the use of moulding techniques for the development of insulin-loaded dissolvable MN systems. Wang *et al.* introduced a bioinspired MN system consisting of dissolvable cross-linked poly(vinyl alcohol) (PVA) gel, catalase and glucose oxidase (GOx) that responds to high glucose conditions by releasing insulin to the circulation. *In vivo* tests showed that the systems were effective in maintaining normal blood glucose levels [11]. In another study, modified alginate and hyaluronate were combined into a dissolvable, insulin-encapsulating MN system. The MN arrays demonstrated good mechanical properties and skin penetration capability while clinical studies demonstrated that the MNs almost fully dissolved into the skin. The released insulin achieved a sustained hypoglycaemic effect and good relative bioavailability of insulin, compared with subcutaneous injections [12]. Similar results in terms of mechanical properties, relative insulin bioavailability and pharmacological activity were also obtained by a study that manufactured composite dissolvable MNs [13]. The forenamed studies

63 demonstrate that MN can be a promising alternative to subcutaneous injections for insulin
64 therapy.

65 Nonetheless, there are several hampering parameters that need to be taken under consideration
66 for the development of transdermal insulin delivery systems. The first relates to the time needed
67 for the detection of the drug into the systemic circulation; dissolvable systems are highly
68 dependent on the dissolution rate of the materials encapsulating the drug and may not be suitable
69 for fast insulin administration. To circumvent that issue, Ross *et al*. developed a solid MNs-
70 based system, coated with insulin-containing formulations through inkjet printing [14]. The use
71 of this technology permitted the accurate deposition of uniform and homogeneous coatings, with
72 high reproducibility. The implementation of inkjet printing for the development of thin layers on
73 the microneedle surface resulted in rapid insulin release within the first 20 min.

74 Another pitfall stems from the use of moulding techniques, that involve a series of multiple,
75 often time-consuming steps. It is evident, that the upscaling of such processes can be
76 challenging. Furthermore, there is a lack of clinical data related to cytotoxicity of materials used
77 for moulded microneedles which actually limits their applications. Another important
78 disadvantage is the limited drug loading in polymeric microneedles without affecting their
79 mechanical properties and piercing capacity. In order to circumvent this issue several authors
80 proposed the use of large patches which in turn results in difficulties to apply the arrays in a
81 uniform manner and subsequently in dose variation of the administrated substances. Recently,
82 efforts have been made on the integration of the revolutionary technology of 3D printing as a
83 manufacturing method for MN-based systems. 3D printing or Additive Manufacturing (AM) is a
84 family of technologies that implement layer-by-layer processes to fabricate physical models,
85 based on a Computer Aided Design (CAD) model. 3D printing permits the fabrication of high

degrees of complexity with great reproducibility, in a fast and cost-effective fashion [15–18]. In the field of transdermal drug delivery systems, the use of photopolymerization-based techniques such as Stereolithography (SLA), Digital Light Processing (DLP) and Two-Photon-Polymerization (2PP) for the development of MNs has been reported [19–22]. Gittard *et al.* fabricated MNs of various geometries for wound healing applications using a DLP system. The MNs were then coated with silver and zinc oxide thin films by pulse laser deposition and their antimicrobial character was verified [23]. In another study, drug-loaded MNs were developed when a skin anticancer drug was incorporated into the photo-sensitive polymer blend prior to photopolymerization through a micro-stereolithographic (DLP) apparatus [24].

In this study, 3D printed MN arrays featuring two different MN designs, pyramid and spear, were developed employing a commercial SLA printer and a biocompatible Class 1 polymer. The 3D printed arrays were subsequently coated with insulin–sugar films using inkjet printing. Mannitol, trehalose and xylitol were used as insulin carriers to preserve insulin activity prior to the deposition of active films on the MNs surface. *In vitro* and *in vivo* studies demonstrated rapid insulin release from the coated MN systems. The usage of SLA for 3D printing of microneedle arrays is anticipated to overcome the existing disadvantages of conventional techniques by providing high precision, rapid fabrication, reduced processing steps and freedom to print a wide range of shapes.

Materials and methods

Materials

The insulin employed in this study was bovine and was procured in a 10 mg mL^{-1} solution from Sigma-Aldrich (Gillingham, UK). Xylitol (Xylisorb® 90) and mannitol (Pearlitol®) were

donated by Roquette Freres (France) while trehalose dihydrate was bought from Sigma-Aldrich (Gillingham, UK). The resin used to fabricate the MNs was the biocompatible Class I resin, Dental SG, by Formlabs. Streptozocin (≥75% α-anomer basis, ≥98%) and citric acid were both purchased from Merck Chemical Co. (Darmstadt, Germany). All solvents were of analytical grades.

Additive manufacturing of microneedles

The MN arrays were designed using an engineering software (SolidWorks, Dassault Systems) as patches of 15x15x1 mm. The patches featured two different needle shapes, a pyramid and a flat spear shaped that geometrically resembled the shape of metallic MNs that has been studied elsewhere [16]. This design, named 'spear' in the framework of this study, had base dimensions of 0.08x1 mm, while the dimensions of the base for the pyramid MN were 1x1 mm. The length of all MNs was 1 mm and all patches had a 6x8 needle layout, yielding 48 MNs per patch. The arrays were 3D printed using the Form 2 SLA printer by Formlabs with high resolution capabilities (25 and 140 microns for z and x axes, respectively). After fabrication, the arrays were washed in isopropyl alcohol bath to remove unpolymerized resin residues and then cured for 60 min at 40 ^{o}C under UV radiation using the MeccatroniCore BB Cure Dental station.

Coating of microneedles through inkjet printing

An inkjet printer was employed (NanoPlotter II, Gesim, Germany) to print thin insulin-sugar films on the surface of the 3D printed MNs. The inkjet printer forms the drug-containing films depositing multiple layers of insulin – sugar droplets on each microneedle using a piezo-driven dispenser (PicPip 300). In each coating cycle (layer), the dispenser jetted 2 droplets of

130 formulation in 10 spots along each needle's longitudinal axis. A total of 92 coating cycles
131 resulted in a 10 UI (350 μg) of insulin per array. The coated arrays were then incubated at room
132 temperature for 24 hours to allow the evaporation of the solvent (de-ionised water) and the
133 formation of uniform films. For the purposes of this study three coating formulations were used,
134 consisting of insulin:xylitol (5:1 wt/wt), insulin: mannitol (5:1 wt/wt) and insulin:trehalose (5:1
135 wt/wt) as 2% solid content. Prior to the coating process, the arrays were mounted on a metal stub
136 at 45^{o} relative to the dispenser, while its tip (50 μm) was placed close to the MN surface to avoid
137 losses of material.

138 Scanning electron microscopy (SEM)

139 The coated MN arrays were mounted onto aluminium stubs using a double-sided carbon
140 adhesive tape (Agar Scientific, UK). Each coated MN array was examined by SEM (Hitachi SU
141 8030, Japan) using a low accelerating voltage (1.0kV). A low accelerating voltage was used to
142 avoid electrical charges on the MNs. The images of coated MNs were captured digitally from a
143 fixed working distance (11.6 mm) using different magnifications (e.g. 30, 80, 110 or 120 x).

144 X-Ray Computer Micro Tomography

145 X-Ray Micro Computer Tomography (μCT) scans were performed on coated 3D printed
146 pyramid MN. The equipment employed was a Bruker Skyscan 1172, with an SHT 11 Megapixel
147 camera and a Hamamatsu 80kV (100μA) source. The samples comprised of 3D printed pyramid
148 MN coated with the three insulin/sugar formulations; Sample A: insulin:xylitol (5:1 wt/wt),
149 Sample B: insulin: mannitol (5:1 wt/wt) and Sample C: insulin:trehalose (5:1 wt/wt). After the
150 scans of the coated arrays were performed, the arrays were inserted in 8-ply strips of parafilm,
151 applying a force of 5 N, to examine the performance of the coating during piercing and to

investigate whether any coating material will remain on the parafilm surface, causing drug losses. Moreover, the penetration depth was measured. The samples were mounted vertically on a portion of dental wax and positioned 259.4 mm from the source. No filter was applied to the X-Ray source and a voltage of 80 kV was applied for an exposure time of 1,050 ms. The images generated were 2,664 x 4,000 pixels with a resolution of 6.75 μm per pixel.

A total of 962 images were taken in 0.2º steps around one hemisphere of the sample with the average of 4 frames taken at each rotation step. The images were collected and a volumetric reconstruction of the sample generated by Bruker's *CTvol* software. The threshold for this attenuation signal was set manually to eliminate speckle around the sample, and then further cleaned with a thresholding mask using Bruker's *CTAn* software. The images produced by the μCT are based on the level of attenuation though the sample, which is dependent on the thickness of the material and its absorption coefficient. Here, it is assumed that the absorption coefficient is linearly proportional to the density of the material and the resulting densities expressed in Hounsfield Units (HU), with -1000 being the density of air and 0 being the density of water.

Circular Dichroism (CD)

Insulin solution and the respective solutions of the insulin-sugar films were diluted to 1.0 mg mL^{-1} in deionised water and the spectra were recorded at 20 ºC between 190 and 260 nm by CD (Chirascan, Applied Photophysics, UK) using a 0.1 mm polarization certified quartz cell (Hellma). Spectra were recorded using a step size of 1 nm, a bandwidth of 1 nm and an acquisition time of 1 sec. Four scans were recorded for each sample, averaged and a corresponding spectrum of water was subtracted from each spectrum. For estimation of the

secondary structural composition of insulin, the CD spectra were evaluated using the CD SSTR method [25].

Raman Spectroscopy

The films and their respective components were analysed using Raman microscopy (Jobin Yvon LabRam I) with a laser of 532 nm wavelength coupled with an optical microscope with 50x objective.

Penetration studies through porcine skin

The effect of the MN geometry on the force required to pierce the skin has been documented [26]. In this study, to determine the effect of needle shape on the force required for skin penetration, piercing tests using porcine skin were conducted. Identical piercing tests were carried out using metallic MN arrays that have been studied and are described in literature [16], to maintain a frame of reference with the respective studies. A texture analyser was employed, and the MN array was mounted on the moving probe using double-sided adhesive tape. Prior to testing, the porcine skin samples were placed in waxed petri dishes. Continuous force and displacement measurements were recorded to identify the point of needle insertion. The speed of the moving probe was 0.01 mm s^{-1}.

Axial force mechanical testing of MNs

To evaluate the mechanical behaviour of the 3D printed microneedles, fracture testing under axial loading was performed. The arrays were fixed onto a metal plate and were pressed against a flat metal block attached to the moving head of a Tinius Olsen testing machine, until a pre-set displacement of 500 μm (height/2) was reached. Continuous force and displacement

194 measurements were recorded to identify the point of needle failure. The speed of the moving
195 probe was 1 mm/s and the experiments were replicated 5 times for each design.

196 Preparation of porcine skin for in vitro release of insulin

197 The release of insulin from the coated MNs through abdominal porcine skin was studied using
198 Franz diffusion cells (PermeGear, Inc., PA, USA). The full thickness abdominal porcine skin
199 was collected from a local slaughterhouse (Forge Farm Ltd, Kent, UK) and was then shaved
200 using a razor blade. The fatty tissue below the abdominal area of porcine skin was removed with
201 scalpel and then pinned onto polystyrene block and wiped with 70 % ethanol. The skin was then
202 cut by applying the dermatome at an angle of ±45° (Padgett dermatome, Integra LifeTMSciences
203 Corporation USA). The thickness of the skin was measured by using a calliper and the tissue
204 disks of the required dimensions were cut for the Franz diffusion cells using a scalper. The skin
205 tissue (1.0 ± 0.1 mm thick) was placed onto filter paper soaked in a small amount of saline
206 phosphate buffer (pH 7.4) for 2 h.

207 In vitro release of insulin through porcine skin

208 A total diffusion area of 1.1 cm^2 was used to assess the insulin release. The MN arrays were
209 inserted into the abdominal porcine skin samples for 30 s, via manual finger pressure. The
210 sample was then mounted onto the donor compartment of a Franz diffusion cell. The temperature
211 of the Franz cells was maintained at 37ºC using an automated water bath (Thermo Fisher
212 Scientific, Newington, USA). Sample fractions (6-6.5 mL h^{-1}) were collected using an auto-
213 sampler (FC 204 fraction collector, Gilson, USA) attached to the Franz diffusion cells system.
214 Statistical analysis for the drug release was performed by using a Mann-Whitney nonparametric

test and t-test analysis for the in vivo studies (InStat, GraphPad Software Inc., San Diego, CA, USA), where samples were considered as statistically significant at $p < 0.05$.

High-Performance Liquid Chromatography (HPLC)

The amount of insulin collected from the receptor fluid was determined by HPLC (Agilent Technologies, 1200 series, Cheshire, UK) equipped with a Phenomenex Jupiter 5u c18 300 Å, LC Column (250×4.60 mm, particle size 5 µm, Macclesfield, UK). The mobile phase consisted of water with 0.1 % Trifluoroacetic Acid (TFA) and acetonitrile with 0.1% TFA (66:34v/v), with a 1 mL min^{-1} flow rate. The column was equilibrated at 35°C, the injection volume was 20 µL and the eluent was analysed with a UV detector at 214 nm. The results were integrated using Chemstation® software and the samples analysed in triplicates.

In vivo release in diabetic mice

Prior to the induction of diabetes, Swiss albino female mice (120 ± 10 g) were allowed free access to solid bottom cages with controlled diet and water for 3 days. Mice were subcutaneously injected on the flank with streptozotocin (70 mg kg^{-1}) in citric acid buffer (pH 4.5) to produce a diabetic animal model. To confirm the induction of diabetes, the fasting blood glucose level was measured at scheduled times using a one-touch glucometer (ACCU-CheckVR Active, Roche, Germany). After one week, mice with blood glucose exceeding 300 mg/dl were considered as diabetic. The diabetic animals were anesthetised and shaved carefully using an electric razor (Panasonic, USA) 24 hours prior to the experiments. Furthermore, the diabetic mice were fasted for 12 hours before the beginning of the study, receiving only water and libitum. The mice were randomly divided into three groups (n=3 for each group): (1) untreated group as negative control; (2) subcutaneous injection (SC; 0.2 IU/animal) as positive control; (3) 3D printed MN (0.2

IU/array). The 3D printed MN arrays were applied onto the dorsal skin of the animals using adhesive tape (3M, USA) to prevent any dislodgement during therapy. After 2 hours, the 3D printed MN patches were removed. For all groups, blood samples were collected from the jugular vein at 0, 1, 2, 3 and 4 hours after the insulin administration and the blood glucose level was measured using the glucometer mentioned. Plasma insulin concentrations were measured via an insulin-EIA Test kit (Arbor Assays, MI, USA). The treatment strategy is described in Table 1.

All animal experiments throughout this study were approved by the Research Ethics Committee (reference number 0003/17, Department of Pharmacy, Southern University Bangladesh) and conducted according to the Southern University Bangladesh policy for the protection of Vertebrate Animals used for Experimental and Other Scientific Purposes, with implementation of the principle of the 3Rs (replacement, reduction, refinement). No skin reactions to MNs occurred.

Pharmacodynamic and pharmacokinetic profile of insulin-coated 3D printed MNs

The minimum glucose level (Cmin) and the time point of minimum glucose level (Tmin) were calculated from the plasma glucose level versus time curve. The relative pharmacological availability (RPA) was calculated using equation 1.

$$RPA(\%) = (AAC3DMN \times dosesc) / (AACsc \times dose3DMN) \times 100 \quad \text{(Eq.1)}$$

Where AAC3DMN indicates the area above the curve after the application of the insulin-coated 3D printed MNs, and AACsc shows the area above the curve after the subcutaneous injection of insulin.

The maximum plasma insulin concentration (Cmax) and the time point of maximum plasma insulin concentration (Tmax) were calculated from the plasma insulin concentration (μIU/ml) versus time curve. The relative bioavailability (RBA) was determined using equation 2.

$$RBA(\%)=(AUC3DMN \times dosesc)/ (AUCsc \times dose3DMN) \times 100 \quad \text{(Eq.2)}$$

Where AUC3DMN indicates the area under the curve after the application of the insulin-coated 3D printed MNs, and AUCsc shows the area under the curve after the subcutaneous injection of insulin.

Results and Discussion

Additive Manufacturing and printability of microneedles

MN arrays featuring pyramid and spear needles were 3D printed using a commercial SLA printer based on digital CAD designs developed via appropriate engineering software. The polymer employed was a photo-sensitive Class I resin which has been FDA approved. All arrays were washed and subsequently cured under UV radiation in a controlled temperature environment to improve the material's mechanical performance.

The capability of 3D printing technology to manufacture complex structures reproducibly and accurately in a one-step-fashion, was exploited in this work to build different designs of MN arrays. Although the degree of complexity that can be achieved through 3D printing is often not achievable through many conventional techniques of MN manufacturing, the technology is hampered by restrictions in terms of resolution that can affect the formation of sharp MN tips. Conventional low-budget SLA printers have a maximum resolution of 100 microns that is governed by the size of the laser focal point and restricts the minimum size of MN tip that can be

formed. The MNs designed in the framework of this study featured a tip of 100 microns by design and their penetration capability through porcine skin was tested to verify that they will successfully and painlessly pierce the skin.

The printability of MNs was further improved when printing-in-an-angle was implemented, leading to finer, sharper MN tips. An innate characteristic of the SLA technology is the interdependence between the print quality and the cross-sectional area in the z-axis; the smaller the z-axis cross-sectional area, the better the quality. This stems from the peel-off function of the printing process, according to which, after the completion of each layer, a wiper slides and peels the structure off the bottom of the resin tank. Larger z-axis cross sectional areas lead to greater forces applied by the wiper, which can deform the printed structures. Orienting the part to minimise the contact area of the structure to the resin tank avoids the possible distortions during the peel-off process and leads to better print quality.

SLA parts are considered mechanically isotropic which ensures the mechanical properties of the arrays are not affected by the angle of printing. In addition, an influential factor of the mechanical performance of the MN arrays is the selection of post-process curing parameters (time and temperature). Further research is required to determine the effect of those factors on the overall mechanical and piercing behaviour of the MN arrays. In this work, the MNs were cured in a UV chamber for 60 min in temperature of 40 ^{o}C. It is demonstrated in this study that those parameters yielded systems that successfully pierced through porcine skin requiring small forces, with no needle failure occurring.

As discussed above due to technical limitations of the existing MN manufacturing techniques (e.g. moulding, lithography) such as limited drug loading, dose consistency and scalability issues

300 there are no commercialized products. Polymeric MNs are fabricated using moulding approaches
301 while metal MNs implement dip – coating techniques which renders both approaches impractical
302 for large scale manufacturing. In contrast scale-up of SLA printed MNs is directly related to the
303 usage of large volume printers or the in-line arrangement of existing printers. We envisage that
304 the implementation of SLA printed MNs will open new horizons for transdermal drug delivery
305 due to the low cost of the printers, printing inks and fast fabrication times.

306 SEM analysis demonstrated that through the use of the SLA technology, uniform and
307 reproducible arrays were developed (Fig. 1a,b). In Fig. 1, the high consistency and
308 reproducibility of the MN layers is depicted, and the formation of sharp tips is demonstrated. It is
309 evident, that the high-resolution capabilities of the printer allowed the parallel fabrication of
310 identical and reproducible arrays with characteristics that favour the skin insertion.

311 Coating of microneedles through inkjet printing

312 Insulin and sugar alcohol coatings were formed on the surface of the 3D printed MNs using
313 inkjet printing and a piezoelectric dispenser. A similar process was developed in earlier studies
314 for coating metallic MNs [16,27], where the applied voltage (mV) and pulse duration (ms) were
315 tuned to achieve the production of droplets of 300 pL volume with particle size of 100-110 μm.
316 Fig. 1c,d illustrates the uniformity and reproducibility of the coatings on the MN surface without
317 any losses of material in the form of satellite droplets on the substrate. Moreover, it is
318 demonstrated that the consecutive jetting cycles produced drug-containing films that are smooth
319 and level in comparison to other techniques such as dip coating that may yield voluminous and
320 inconsistent coatings. This smooth morphology of the films prevents the losses of drug during
321 MN insertion that occur when bulky coatings remain on the skin surface.

The drug carriers selected were two alcohol sugars (xylitol, mannitol) and a disaccharide (trehalose). Those excipients have been reported to favour the immediate coating dissolution in the skin and to enhance insulin stability in solid state [28–30] .

X-Ray Computer Micro Tomography

The coated 3D printed pyramid MN arrays were scanned using the Bruker Skyscan 1172 and an overview of the array is presented in Fig. 2a. For sample A, an average needle base area of 1.095 mm^2 and an average needle height of 1.034 mm were measured. For samples B and C, the average needle base areas were measured as 1.065 mm^2 and 1.091 mm^2 and the average needle heights as 1.040 mm and 1.038 mm, respectively. The average interspacing of the pyramids between the centre points was 1.842 mm, 1.865 mm, and 1.864 mm between columns, and 1.788 mm, 1.810 mm, and 1.796 mm between rows for samples A, B and C respectively. Scans taken from the left-hand side of the arrays illustrate the thin coating films fabricated through inkjet printing, in comparison with respective ones taken from the back side of the array (Fig. 2b,c).

The relative density of the MNs relative to the control sample (uncoated 3D printed pyramid MNs) showed an increase of approximately 200 HU between all coated samples and the control (Fig. 3a,b). Profile lines across a row of MNs revealed a coffee-ring effect in the density of the coating material deposition. While denser material was distributed randomly within each of the MNs, a fringe layer of 10-15 μm was apparent with the effect being most pronounced in the insulin:xylitol coated sample (Fig. 3c).

Penetration experiments in 8-ply strips of parafilm were performed applying a 5 N force (Fig. 4). The penetration depth was measured as 559 μm, 662 μm and 650 μm for samples A, B and C,

343 respectively. The μCT scans illustrate that the coating stays on the MN surface throughout the
344 piercing process and there is no material remaining on the parafilm surface.

345 Circular Dichroism

346 Circular dichroism (CD) spectroscopy is a reliable technique for the evaluation of the secondary
347 structure of proteins in a solution. The influence of the two polyols and the disaccharide on
348 insulin molecule as well as their interactions were studied using CD and the estimation of insulin
349 secondary structure was performed by CDSSTR method [31,32].

350 The far-UV CD spectra of insulin and insulin-sugar films (Fig. 5a) were found to be coincident
351 with the one of standard insulin solution, showing double minima around 210 and 222 nm which
352 are typical of predominant α-helix structure proteins as already reported elsewhere [28,33–35].
353 However, a slight decrease in Molar ellipticity is noted when insulin solution is dried which is
354 also supported by the decrease of the estimated percentage of α-helix and increase of the β-sheet
355 content. Such behaviour may be indicative of the unfolding tendency of insulin during
356 dehydration [36]. Interestingly, once the sugars were added, all the respective insulin-sugar films
357 spectra showed higher Molar intensities than the insulin film alone, indicating an increase in the
358 α-helix content. The protective property of those sugars can be explained by the water
359 replacement mechanism which proposes that sugars may maintain the three-dimensional
360 structure of proteins by hydrogen-bonding with them [37,38]

361 Among the tested sugars, xylitol presented the best capability to maintain insulin in its native
362 secondary structure with even higher amounts of α-helix content. The reason for this still remains
363 unclear and further research is needed.

364 Raman Spectroscopy

In this work, the Raman spectrum of native insulin shows a strong peak at 1661 cm^{-1} due to the amide I mode of α-helix structure and a shoulder at 1682 cm^{-1} which is attributed to random coil form as previously reported by Yu et al. [40]. Distinctive peaks of sugars were not found in Raman mainly because insulin was 5 times more concentrated than the sugars in the films. Likewise, the amorphous nature of the dried formulation (XRD analysis - data not shown) is unlikely to afford a strong Raman signal.

Overall, insulin-sugar formulations showed similar Raman spectra to the native insulin (Fig. 5b). Nonetheless, a slight shift in amide I band position can be seen for all formulations. Amide I band of insulin-xylitol and insulin-mannitol formulations was shifted towards greater frequency, 1663 cm^{-1} and 1662 cm^{-1}, respectively, while insulin-trehalose band was shifted to lower frequency at 1658 cm^{-1}. Those events were also reported by Carpenter and Crowe [37] and Souillac et al. [41], who described that those changes might be due to the different effect of each sugar on the vibrational spectra of insulin as well on the hydrogen bonding and couplings between the adjacent peptide units.

Many researchers have investigated the protective properties of different sugars on polypeptides, proteins and biomolecules [42–44]. It has been advocated that protein aggregation and denaturation can be prevented by using carbohydrates as protectants. Protein protection by the sugars in a dried system can be explained by the water replacement mechanism which suggest the sugars may substitute water molecules around the biomolecules of proteins, maintaining its three-dimensional structure by providing sites with hydrogen-bonding species [37,45,46].

Zeng *et al.* studied the impact of relative humidity (RH) on dehydration of insulin crystals and they found the hydration water from insulin crystal can be gradually excluded when the RH is

387 decreased. They used the high frequency region in Raman spectroscopy to access the band at
388 ~3450cm^{-1} which is caused by both water and amino acid residues with O-H groups. A
389 continuous dropping of the O-H stretching band around 3450 cm^{-1} was observed while the RH
390 was reduced, indicating dehydration of the molecule [47].

391 From Fig. 5b it can be seen that for all formulation the S-S vibration bands are located close to
392 513 cm^{-1} suggesting that all disulphide bonds are in an adopted more stable gauche – gauche -
393 gauche conformation [47,48] as a result of the complete water removal during inkjet printing.
394 Tyr residues present Raman peaks at 642, 828, 852, and 1174 cm^{-1}, while the 1206 cm^{-1} peak is
395 related to both Tyr and Phe residues. Furthermore, the ratios of $I_{852/I828}$ and $I_{1174/I1206}$ varied from
396 0.91 – 1.02 and 0.77 – 0.81 respectively. These values are much lower compared to those
397 observed from Zeng et al. [47], for insulin crystals at very low RH (2%). This phenomenon
398 suggests significant water loss of the coated formulation and stronger H – bonding interactions.

399 Vibrational modes in the area of 1100 – 1300 cm^{-1} have shown to be sensitive to the changes of
400 hydrogen bonds which involve the phenolic hydroxyl groups of Tyr residues and particularly the
401 $\nu_{7á}$ frequency. In Fig. 5b the $\nu_{7á}$ has a frequency of 1275cm^{-1} which is a robust evidence that the
402 phenolic OH group of Tyr is strongly hydrogen bonded to a base atom [49].

403 Penetration studies through porcine skin

404 The 3D printed pyramid and spear shaped MN arrays were tested for their porcine skin
405 penetration capability using a texture analyser. Identical experiments were performed using
406 metallic MNs and the results were compared to the respective ones obtained from the 3D printed
407 MN experiments. All piercing tests were successful with no MN damage or failure. Throughout
408 each test, measurements of force and displacement were taken (Fig. 6a).

All curves presented an initial linear segment (displacement < 0.3 mm); after that, the slope was changing constantly until a maximum force value was reached and a steep decrease of the force was observed. This value is identified as the maximum force required for MN insertion [26]. The non-linear behaviour of the force-displacement curve indicates that the process of MN insertion to the skin is comprised of small penetrations where the MNs gradually tear the skin, before the load reaches the maximum value that makes the insertion abrupt [50]. The maximum force required for the MNs to successfully pierce the skin plays a crucial role when different MN designs need to be compared. As presented in Fig. 6b, the pyramid MN required the least amount of force to penetrate the porcine skin.

Axial force mechanical testing of MNs

The two studied MN designs were tested under compressive axial loading to determine the force of microneedle fracture as a function of geometry. The force vs displacement measurements and respective fracture strength values are presented in Fig. 7.

The two designs exhibited different mechanical behaviours during testing. For both designs, the recorded force increased until the ultimate load was reached, and fracture occurred. For the spear MNs, the point of fracture appears as a peak at approximately 175 N, followed by a drop of the recorded load; as the MNs were kept being pressed against the metal block after fracture, the load was considerably decreased. On the contrary, the pyramid geometry showed a discontinuity at approximately 457 N which is identified as the point of initial needle failure. Afterwards, the load kept increasing as the microneedles kept being compressed. This difference in mechanical behaviour is attributed to the different modes of needle failure. On the one hand, the spear MNs fractured in the lateral direction, perpendicular to the loading axis, a finding that was confirmed

by visual observation. This mode of failure was expected, due to the small thickness of the MNs in that direction, which translates to minimisation of area, thus increased stress fields. On the other hand, the pyramid MNs failed under pure compression, with the tip failing first and additional, increasing force required for the compression of the remaining MN body. These findings verify that both designs are safe for application since the fracture strengths of the arrays are far greater than the respective forces needed for needle penetration through porcine skin. They also confirm that the pyramid geometries present the best potential between the two studied designs.

In vitro release of insulin through porcine skin

The in vitro insulin release studies from 3D printed pyramid and spear MNs were investigated using porcine skin in Franz cells. The used carriers, mannitol, trehalose and xylitol not only preserved insulin in its native form but also provided fast dissolution rates. As shown in Fig. 8a,b for the pyramid designs approximately 80% of insulin was released in the first 2 min with 86 – 92% within 8 min. The rapid release profiles were obtained for all insulin carriers and no statistical difference was observed (two-tail $p = 0.0021$).

The coating of each pyramid side resulted to higher surface area exposed for hydration and thus faster hydration rates. In contrast, the spear 3D printed designs presented slightly slower insulin release rates with 62 – 70% and 81 – 84% released within 2 min and 8min respectively. Overall, the rapid insulin release rates of the 3D printed MNs was attributed to the hydrophilic nature of the three carriers and the thin coating layers (10 – 15μm) as shown from the μCT analysis.

In vivo transdermal delivery of insulin in diabetic mice

Diabetes was successfully induced in mice after 7 days of streptozotocin administration. The preliminary diabetes (hyperglycemia) was demonstrated as 340 ± 10 mg/dl. The diabetic mice were divided into three groups: Untreated (negative control), subcutaneously (SC) injected (positive control) and treated with the 3D printed insulin-coated MNs. Fig. 9 shows the application process of the 3D printed MN arrays.

The dose 0.2 IU/array was selected in order to avoid hypoglycaemia in mice for 4 h. The comparative studies on different delivery strategies in plasma glucose levels are shown in Fig. 10a. Insulin-coated 3D printed MN arrays showed a remarkable steady state hypoglycaemia effect (32.8% from total value) in comparison to negative and positive control. After an hour, subcutaneous injection (0.2 IU/injection) facilitated a rapid increase in insulin concentration in blood and hence the decrease in plasma glucose level was approximately 30.1% from its primary value. A comparable blood glucose regulation was observed between the SC group and the MN group which was achieved within 1 h [51]. Interestingly, the 3D printed patch presented the same rate to reach its lowest glucose level compared to the SC injection. In similar study biodegradable MN patches Tmin of glucose levels was achieved within 2 h with administrated doses of 5 – 10 IU per patch [13]. The main reason for the faster glucose rates is that in *Zhang et al.* (2018) insulin was encapsulated in moulded MN patches while for the 3D printed patches is applied on the microneedle surface with very hydrophilic thin layers resulting in rapid insulin release. Moreover, previous studies have shown that microneedle injection of insulin to human diabetic subjects was chosen over hypodermic infusion and that pharmacokinetics were faster when insulin was administered to the skin compared to the subcutaneous injections [52].

Although the plasma glucose level versus time profile was similar to previous findings [53–57] the steady state plasma glucose level was maintained up to 4 h while the untreated group

(negative control) remained unchanged (no hypoglycaemia) for the same period. These findings suggest that insulin is being released from the 3D printed MNs to the mice blood stream via passive diffusion to blood capillary.

Fig. 10b illustrates the plasma insulin concentration versus time where both SC and 3D printed MN groups achieved the highest amount of plasma insulin concentration after 1 h of administration. The control group did not show any detectable plasma insulin concentration. The highest insulin level of the 3D printed MNs is slightly lower to the SC injection but no statistical difference was observed. As shown in Fig. 10b after post – administration for 4 h the serum insulin of 3D printed microneedles was higher to the SC injection.

Tables 2 and 3 represent the pharmacodynamic parameters of plasma glucose levels and the pharmacokinetic parameters for plasma insulin concentrations, respectively. The RPA and RBA for the insulin-coated 3D printed MNs group were both about 85-96%. These results indicate that insulin released from 3D printed MNs was almost completely absorbed from the skin into the systemic circulation, and the pharmacological activity of the released insulin remained intact after the delivery with the 3D printed MNs.

Conclusions

MN arrays of high quality and reproducibility, featuring spear and pyramid-shaped needle geometries, were successfully fabricated by a biocompatible resin using stereolithography. The 3D printed polymeric MNs required low forces to penetrate porcine skin, in comparison with metallic MNs. Uniform and accurate insulin-sugar thin layers were applied on the surface of the MNs through inkjet printing, with no satellite droplets detected on the substrate. The insulin integrity was found to be preserved by all carriers, namely the α–helix and β-Sheet, with xylitol

showing the optimum performance. *In vivo* animal trials demonstrated that 3D printed MNs facilitate rapid low glucose levels with longer duration compared to SC injections.

499

500 FIGURES

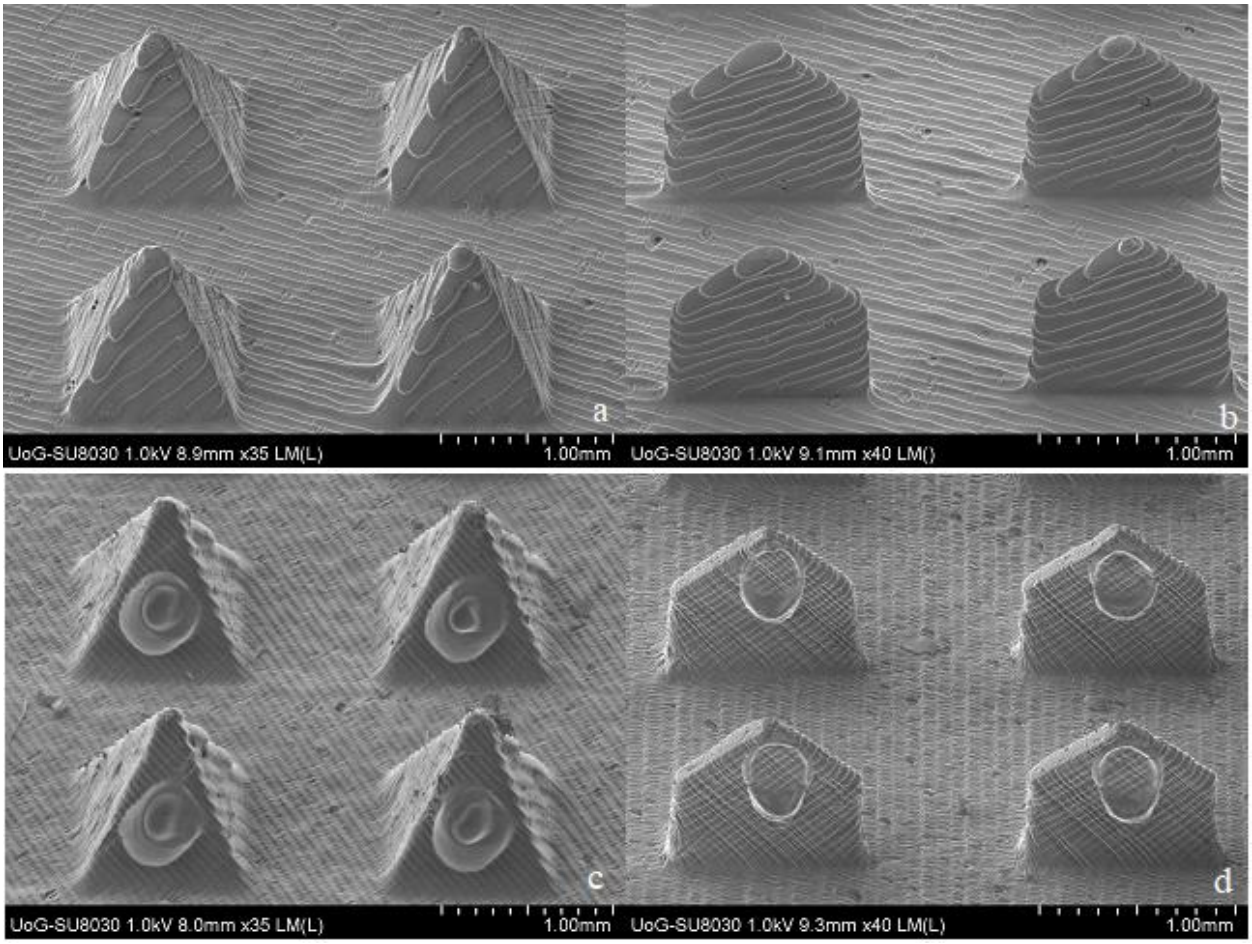

501

502 Figure 1. SEM images of the 3D printed MNs. (a) Uncoated pyramid; (b) uncoated spear; (c)
503 coated pyramid; (d) coated spear. The thin coating films on the MNs were created using an inkjet
504 printer. The formulations employed for the coatings contained insulin and a sugar used as a
505 carrier (xylitol, mannitol and trehalose) in a 5:1 ratio. Each MN patch was coated with 10 IU. All
506 insulin-carrier combinations formed coatings with similar morphology. The carrier used for
507 captions (c) and (d) is xylitol.

508

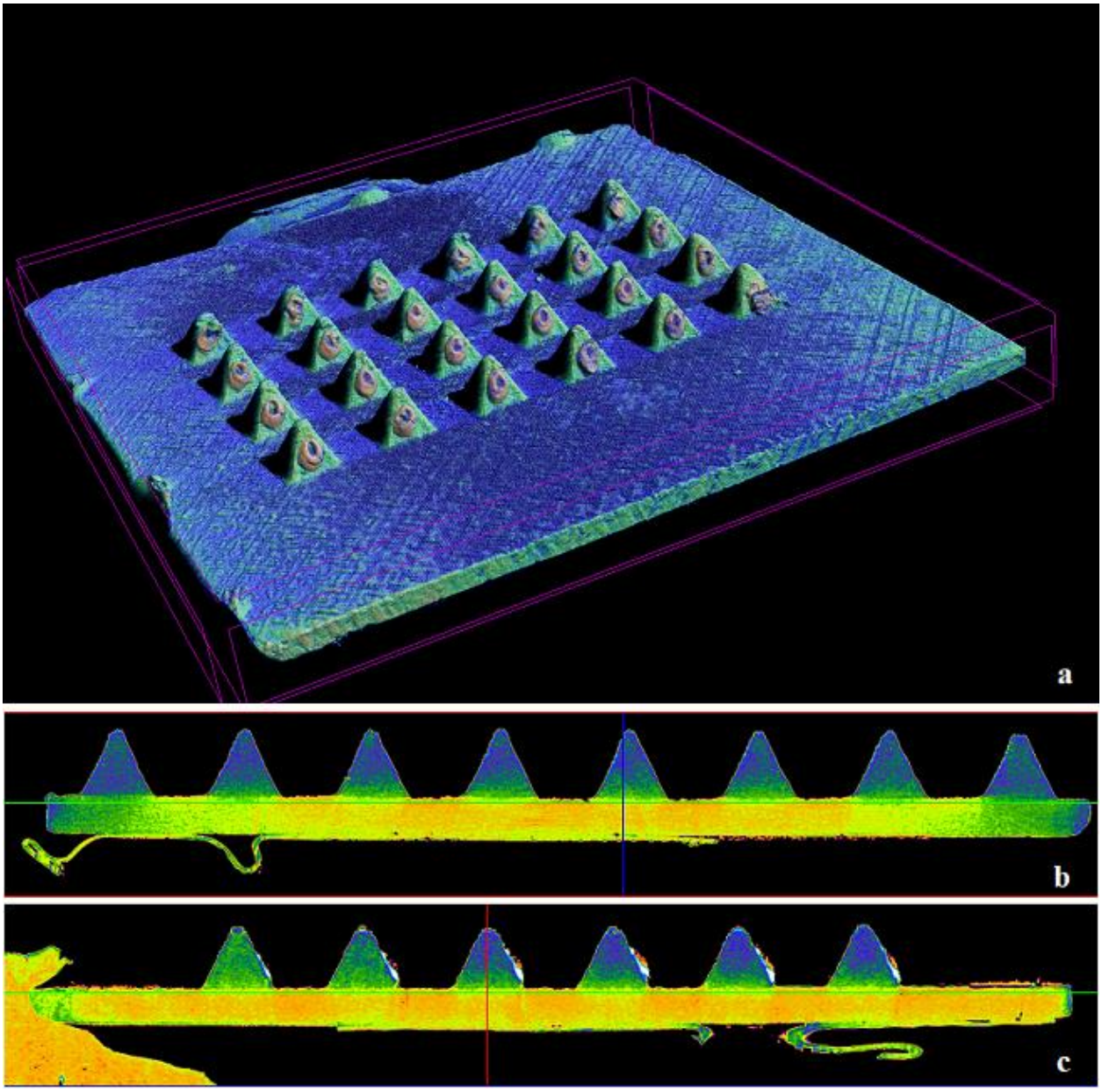

509

510 Figure 2. µCT images of the pyramid MN arrays coated with insulin:xylitol formulation.

511 (a) Overview; (b) image taken from the back side; (c) image taken from the left-hand side of the

512 array, showing the thin film coating.

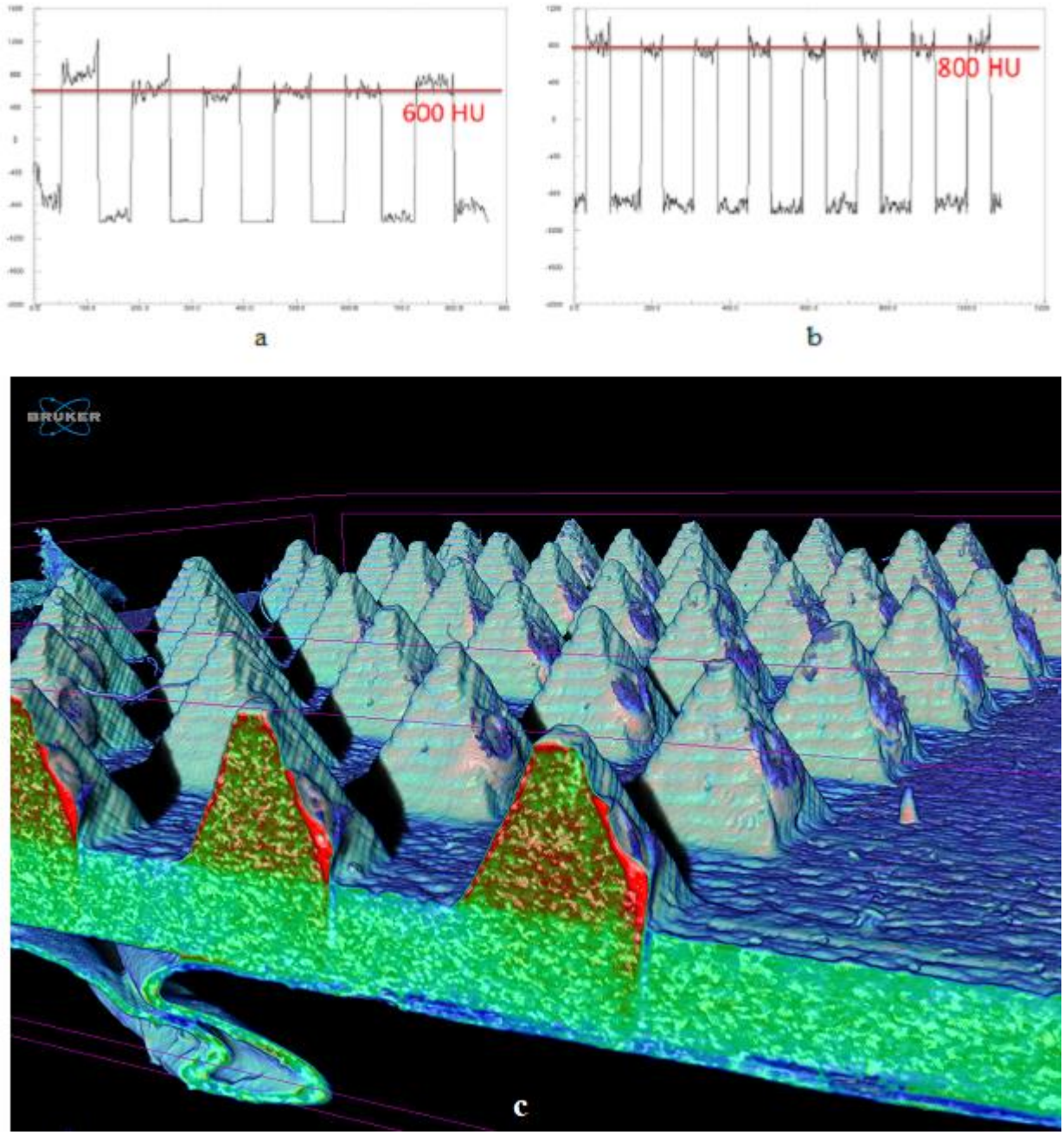

Figure 3. µCT evaluation. (a) Profile lines, measured across a single row of the control sample (uncoated array) and (b) the coated pyramid MN array with insulin:xylitol formulation, showing a 200 HU increase; (c) cross-section of the coated MN array showing a fringe layer of 10-15 µm.

517 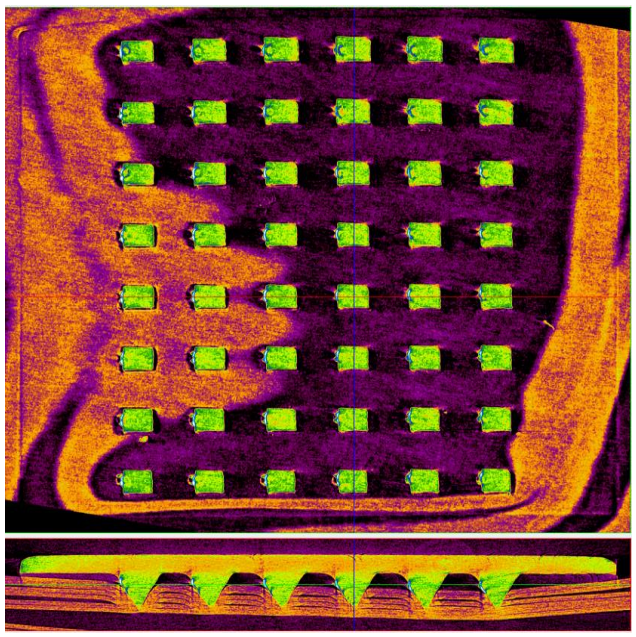

518 Figure 4. Cross section of MN array penetration through 8-ply strip of parafilm, applying a 5N
519 load.

520

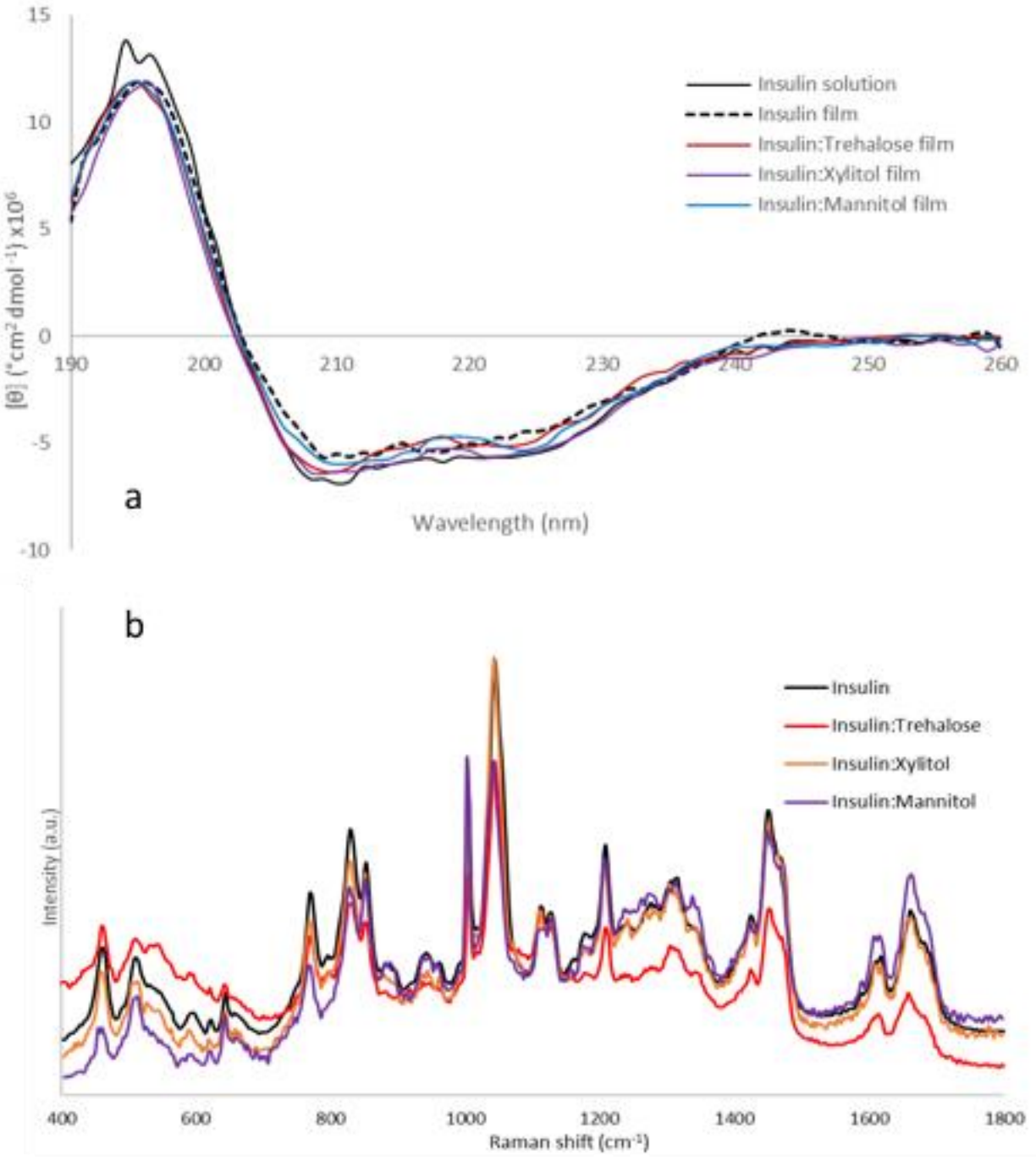

Figure 5. **a)** CD of insulin and insulin formulations and b) Raman spectra from 500 to 1800 cm^{-1} of pure insulin and insulin-sugars.

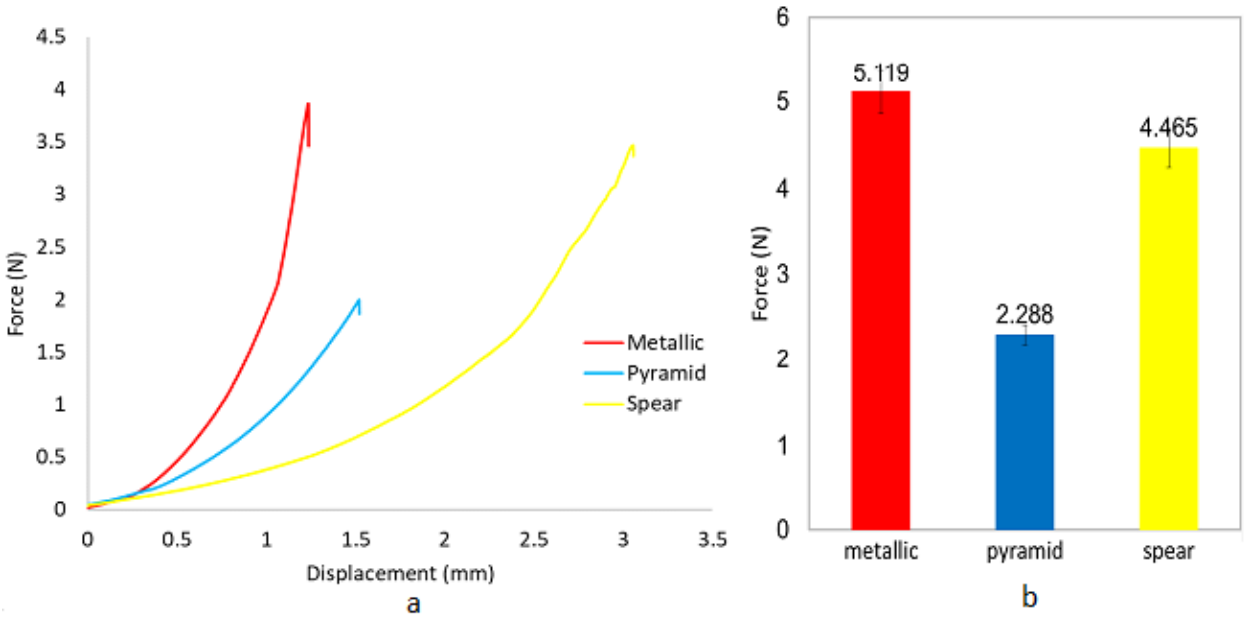

Figure 6. Penetration studies of MNs through porcine skin, comparing 3D printed spear and pyramid designs with metallic MNs. (a) Force against displacement curves recorded during MN insertion tests; (b) Maximum force required for MN penetration.

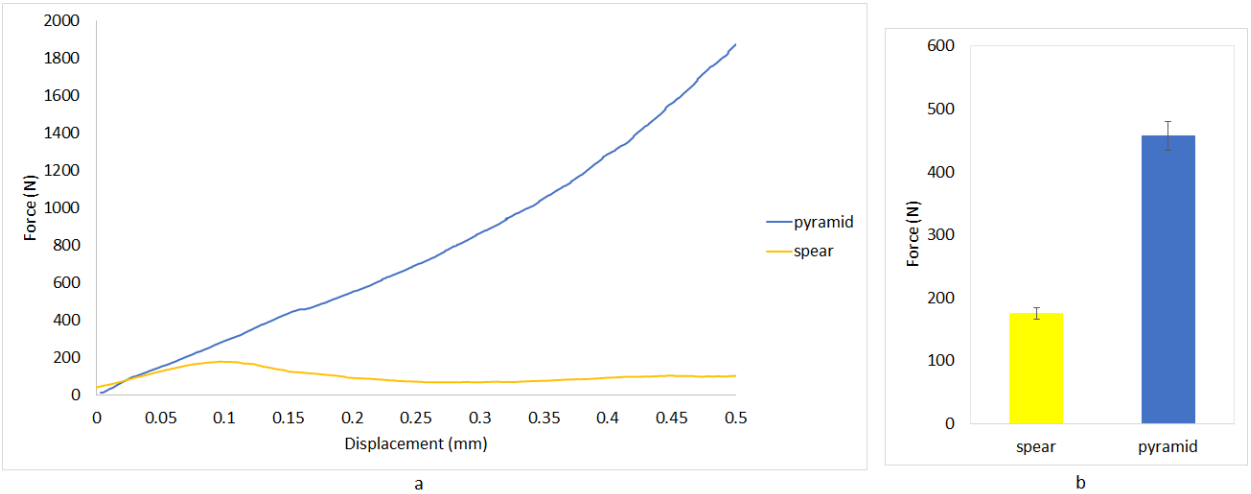

Figure 7. MN fracture testing for pyramid and spear designs. (a) Force against displacement curves recorded during MN fracture tests; (b) Fracture MN strength

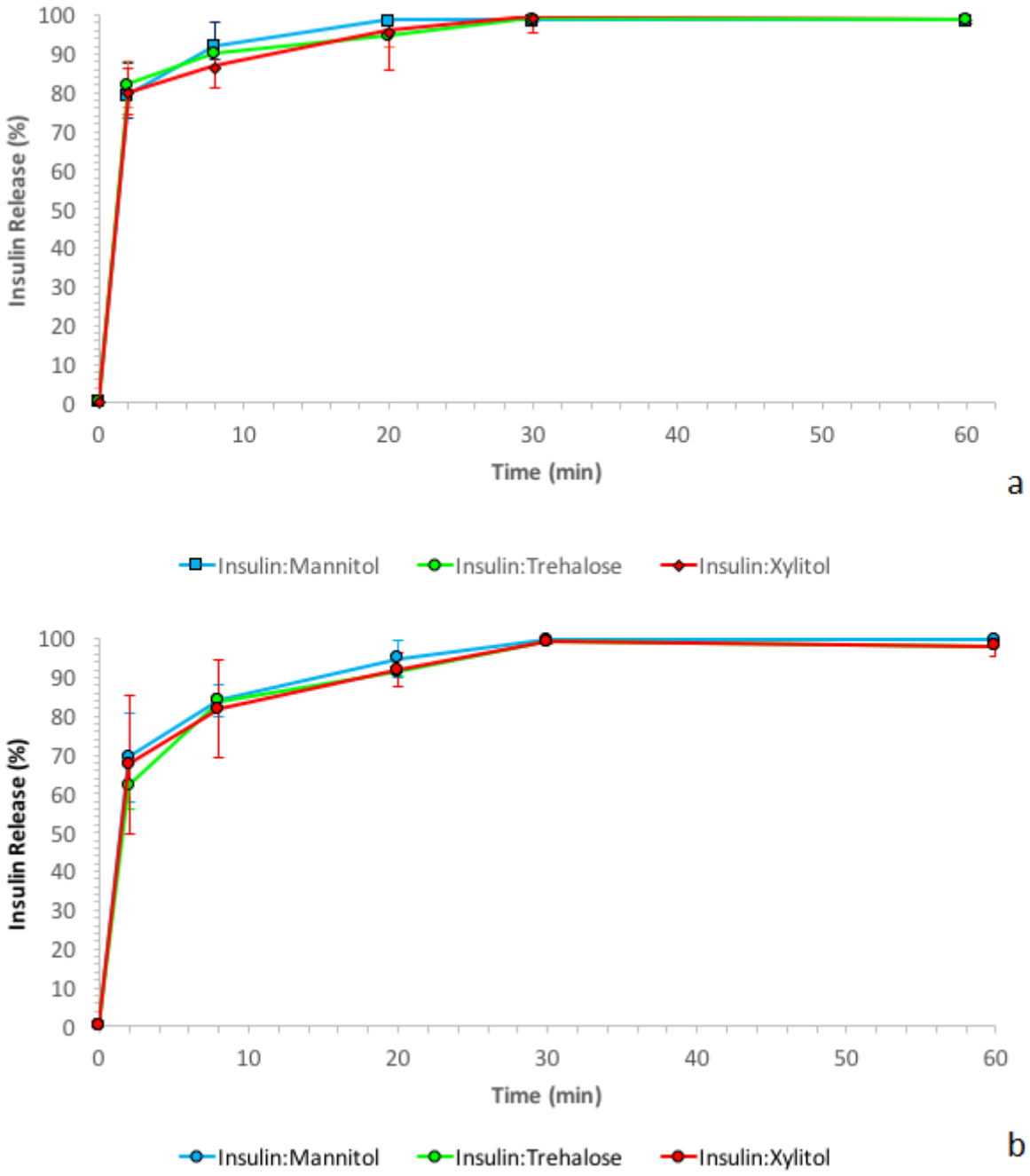

534

535 Figure 8. In vitro insulin release through porcine skin from a) the pyramid and b) the spear MN

536 designs for all investigated drug carriers.

537

Figure 9. Experimental mice (A) before the application, (B) during the application and (C) after removal of the 3D printed MN array for the delivery of insulin to diabetic mice.

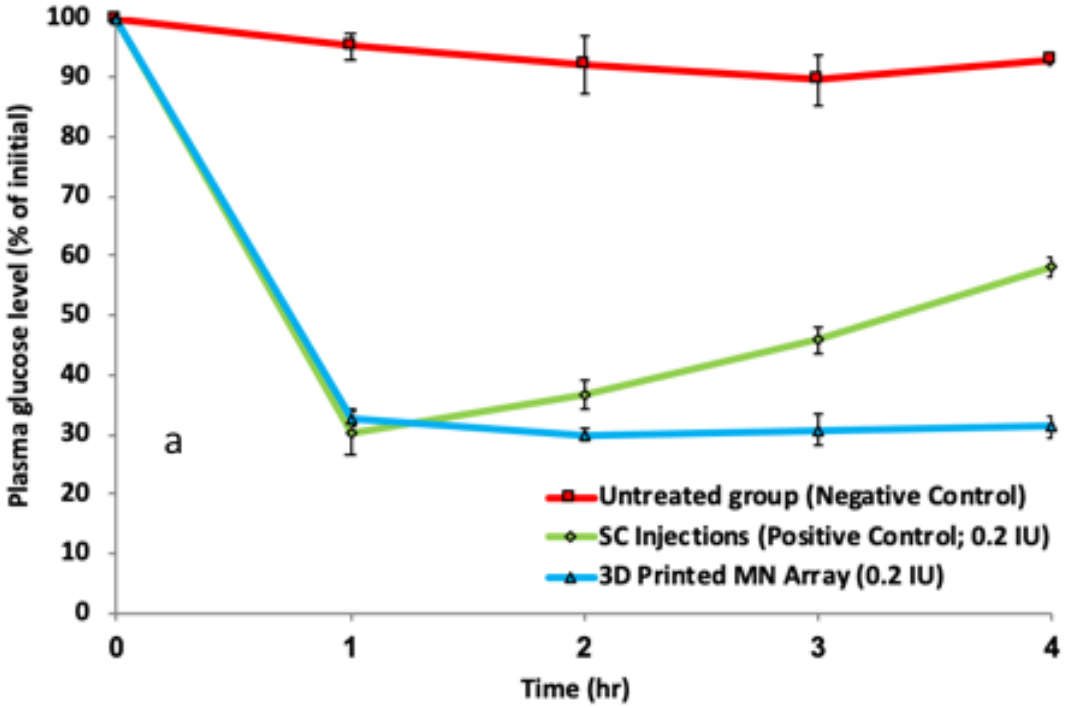

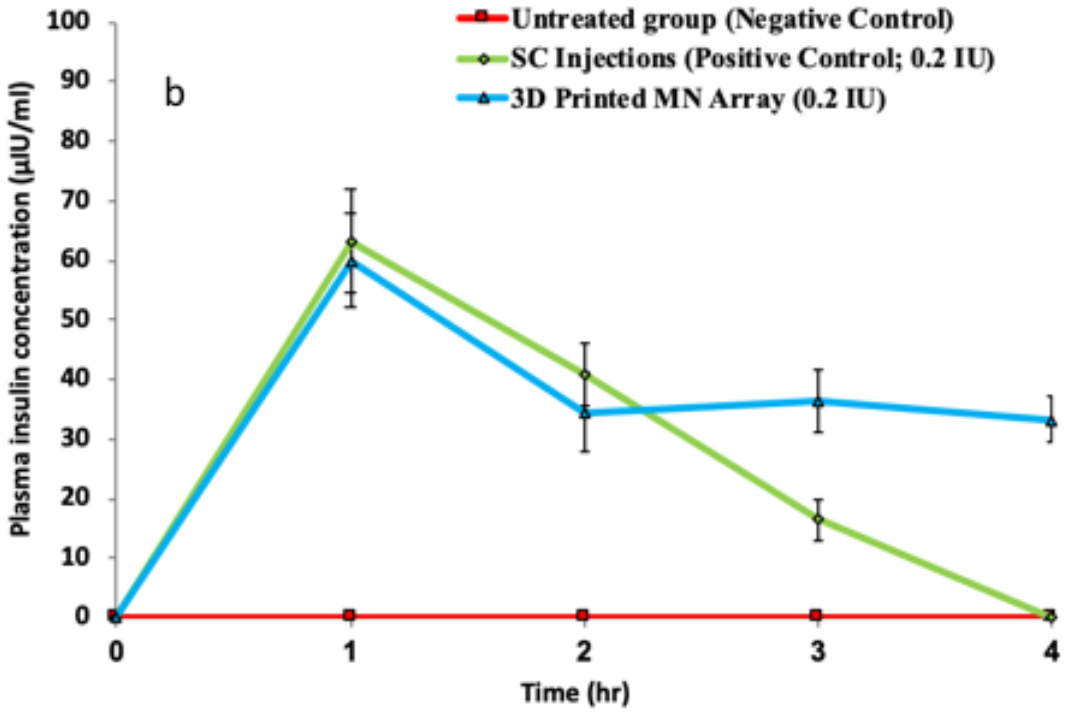

541

542 Figure 10. a) Comparative plasma glucose level vs time for untreated group, subcutaneous (SC)
543 injection and insulin-coated 3D Printed MN array applied to diabetic mice, over 4 hours (n=3),

b) comparative plasma insulin concentration vs time for untreated group, subcutaneous (SC) injection and insulin-coated 3D Printed MN array applied to diabetic mice, over 4 hours (n=3).

TABLES

Table 1 Treatment protocol for insulin-coated 3D printed MN array.

Day	Stage	Treatment strategy
-7	Animal model selection and isolation	Transfer mice to study isolator
0	Induction of diabetes	• Weigh animals and injected with streptozotocin (diabetes inducer) • Daily blood glucose measurements
1		
2		
3	Observation	Blood glucose level measurements
4		
5		
6		
7	Confirmation of diabetes induction	Blood glucose level exceeds 300 mg/dl within 7 days.
8	Antidiabetic therapy using insulin-coated 3D printed MN array	After treatment, hourly (up to 4 hours) blood samples were collected from the jugular vein and the blood glucose level was measured. The study was conducted for 24 hours.

Table 2. Pharmacodynamic parameters for plasma glucose levels of diabetic mice for untreated groups, subcutaneous (SC) injection (insulin dose: 0.2 IU) and 3D Printed MN array (insulin dose: 0.2 IU) (n=3).

Group	C_{min} (%)	T_{min} (h)	$AAC_{0 \text{ to } 4}$ (% hr)	RPA (%)
Untreated groups	89.5 ± 4.2	3	22.7 ± 1.2	-
SC injections	32.8 ± 3.7	1	208.5± 3.7	100
3D Printed MN arrays	30.1 ± 1.0	1	240.6 ± 2.9	122

C_{min}, minimum glucose level; T_{min}, time point of minimum glucose level; $AAC_{0 \text{ to } 4}$, area above the plasma glucose concentration vs. time curve; RPA, relative pharmacological availability compared to subcutaneous injection.

Table 3. Pharmacokinetic parameters for plasma glucose levels of diabetic mice for untreated groups, subcutaneous (SC) injection (insulin dose: 0.2 IU) and 3D Printed MN array (insulin dose: 0.2 IU) (n=3).

Group	C_{max} (µIU ml^{-1})	T_{max} (h)	$AUC_{0 \text{ to } 4}$ (µIUhr^{-1} ml^{-1})	RBA (%)
Untreated groups	0	0	0	0
SC injections	63.2 ± 8.8	1	120.5 ± 6.4	100
3D Printed MN arrays	59.9 ± 7.9	1	147.4 ± 5.8	115

C_{max}, maximum plasma insulin concentration; T_{max}, time point of maximum plasma insulin concentration; $AUC_{0 \text{ to } 4}$, area under the plasma insulin concentration vs. time curve; RBA, relative bioavailability compared with subcutaneous injection.

AUTHOR INFORMATION

Corresponding Authors

* Corresponding Authors: Prof. D.A. Lamprou, E-mail address: d.lamprou@qub.ac.uk, Tel.: +44(0) 2890 97 2617. Prof. D. Douroumis, E-mail: d.douroumis@gre.ac.uk, Tel: +44 (0) 2083 31 8440.

Author Contributions

The manuscript was written through contributions of all authors. All authors have given approval to the final version of the manuscript.

Funding Sources

This work was supported by the Coordenação de Aperfeiçoamento de Pessoal de Nível Superior (CAPES) Foundation - Ministry of Education of Brazil; and the European Research Council under the European Union's Seventh Framework Programme (FP/2007-2013) / ERC (grant number. 615030).

ABBREVIATIONS

Transdermal Drug Delivery, TDD; MN, microneedle; poly(vinyl alcohol), PVA; glucose oxidase, GOx; Additive Manufacturing, AM; UV, ultraviolet; CD, Circular Dichroism; μCT, Micro Computer Tomography; Scanning electron microscopy, (SEM); High-Performance Liquid Chromatography, (HPLC); relative humidity, (RH).

DATA AVAILABILITY

The data will be available on request.

586

587 REFERENCES

588

589 [1] A.Z. Alkilani, M.T.C. McCrudden, R.F. Donnelly, Transdermal drug delivery: Innovative
590 pharmaceutical developments based on disruption of the barrier properties of the stratum
591 corneum, Pharmaceutics. 7 (2015) 438–470. doi:10.3390/pharmaceutics7040438.
592 [2] W. Chen, H. Li, D. Shi, Z. Liu, W. Yuan, Microneedles As a Delivery System for Gene
593 Therapy, Front. Pharmacolocy. 7 (2016) 137. doi:10.3389/fphar.2016.00137.
594 [3] S.T. Sanjay, W. Zhou, M. Dou, H. Tavakoli, L. Ma, F. Xu, X.J. Li, Recent advances of
595 controlled drug delivery using microfluidic platforms, Adv. Drug Deliv. Rev. 128 (2018)
596 3–28. doi:10.1016/j.addr.2017.09.013.
597 [4] L. Goodchild, Could dissolvable microneedles replace injected vaccines?, Mater. Today.
598 18 (2015) 419–420. doi:10.1016/j.mattod.2015.08.005.
599 [5] S. Kaushik, A.H. Hord, D.D. Denson, D. V. McAllister, S. Smitra, M.G. Allen, M.R.
600 Prausnitz, Lack of pain associated with microfabricated microneedles, Anesth. Analg. 92
601 (2001) 502–504. doi:10.1213/00000539-200102000-00041.
602 [6] D.P. Wermeling, S.L. Banks, D.A. Hudson, H.S. Gill, J. Gupta, M.R. Prausnitz, A.L.
603 Stinchcomb, Microneedles permit transdermal delivery of a skin-impermeant medication
604 to humans, Proc. Natl. Acad. Sci. 105 (2008) 2058–2063. doi:10.1073/pnas.0710355105.
605 [7] R.F. Donnelly, T.R.R. Singh, M.J. Garland, K. Migalska, R. Majithiya, C.M. McCrudden,
606 P.L. Kole, T.M.T. Mahmood, H.O. McCarthy, A.D. Woolfson, Hydrogel-forming
607 microneedle arrays for enhanced transdermal drug delivery, Adv. Funct. Mater. 22 (2012)
608 4879–4890. doi:10.1002/adfm.201200864.

[8] M. Korytkowski, L. Niskanen, T. Asakura, FlexPen®: Addressing issues of confidence andconvenience in insulin delivery, Clin. Ther. 27 (2005) S89-100. doi:10.1016/j.clinthera.2005.11.019.

[9] X. Guo, W. Wang, Challenges and recent advances in the subcutaneous delivery of insulin, Expert Opin. Drug Deliv. 14 (2017) 727–734. doi:10.1080/17425247.2016.1232247.

[10] R.J. Narayan, Transdermal delivery of insulin via microneedles, J. Biomed. Nanotechnol. 10 (2014) 2244–2260. doi:10.1166/jbn.2014.1976.

[11] J. Wang, Y. Ye, J. Yu, A.R. Kahkoska, X. Zhang, C. Wang, W. Sun, R.D. Corder, Z. Chen, S.A. Khan, J.B. Buse, Z. Gu, Core-Shell Microneedle Gel for Self-Regulated Insulin Delivery, ACS Nano. 12 (2018) 2466–2473. doi:10.1021/acsnano.7b08152.

[12] W. Yu, G. Jiang, Y. Zhang, D. Liu, B. Xu, J. Zhou, Polymer microneedles fabricated from alginate and hyaluronate for transdermal delivery of insulin, Mater. Sci. Eng. C. 80 (2017) 187–196. doi:10.1016/j.msec.2017.05.143.

[13] Y. Zhang, G. Jiang, W. Yu, D. Liu, B. Xu, Microneedles fabricated from alginate and maltose for transdermal delivery of insulin on diabetic rats, Mater. Sci. Eng. C. 85 (2018) 18–26. doi:https://doi.org/10.1016/j.msec.2017.12.006.

[14] S. Ross, N. Scoutaris, D. Lamprou, D. Mallinson, D. Douroumis, Inkjet printing of insulin microneedles for transdermal delivery, Drug Deliv. Transl. Res. 5 (2015) 451–461. doi:10.1007/s13346-015-0251-1.

[15] R.D. Pedde, B. Mirani, A. Navaei, T. Styan, S. Wong, M. Mehrali, A. Thakur, N.K. Mohtaram, A. Bayati, A. Dolatshahi-Pirouz, M. Nikkhah, S.M. Willerth, M. Akbari, Emerging Biofabrication Strategies for Engineering Complex Tissue Constructs, Adv.

632 Mater. 29 (2017) 1–27. doi:10.1002/adma.201606061.
633 [16] L.E. Visscher, H.P. Dang, M.A. Knackstedt, D.W. Hutmacher, P.A. Tran, 3D printed
634 Polycaprolactone scaffolds with dual macro-microporosity for applications in local
635 delivery of antibiotics, Mater. Sci. Eng. C. 87 (2018) 78–89.
636 doi:10.1016/j.msec.2018.02.008.
637 [17] H. Tayebi, Lobat.; Rasoulianboroujeni, Morteza.; Moharamzadeh, Keyvan.; Almela,
638 Thafar.K.D.; Cui, Zhanfeng.; Ye, 3D-printed membrane for guided tissue regeneration,
639 Mater. Sci. Eng. C. 84 (2018) 148–158. doi:doi.org/10.1016/j.msec.2017.11.027.
640 [18] D. Lam, CXF; Mo, XM; Teoh, SH; Hutmacher, Scaffold development using 3D printing
641 with a starch-based polymer, Mater. Sci. Eng. C. 20 (2002) 49–56.
642 doi:doi.org/10.1016/S0928-4931(02)00012-7.
643 [19] S.N. Economidou, D.A. Lamprou, D. Douroumis, 3D printing applications for transdermal
644 drug delivery, Int. J. Pharm. 544 (2018) 415–424. doi:10.1016/j.ijpharm.2018.01.031.
645 [20] B. Thavornyutikarn, P. Tesavibul, K. Sitthiseripratip, N. Chatarapanich, B. Feltis, P.F.A.
646 Wright, T.W. Turney, Porous 45S5 Bioglass®-based scaffolds using stereolithography:
647 Effect of partial pre-sintering on structural and mechanical properties of scaffolds, Mater.
648 Sci. Eng. C. 75 (2017) 1281–1288. doi:10.1016/j.msec.2017.03.001.
649 [21] D. Pede, G. Serra, D. De Rossi, Microfabrication of conducting polymer devices by ink-
650 jet stereolithography, Mater. Sci. Eng. C. 5 (1998) 289–291. doi:10.1016/S0928-
651 4931(97)00056-8.
652 [22] E.J. Mott, M. Busso, X. Luo, C. Dolder, M.O. Wang, J.P. Fisher, D. Dean, Digital
653 micromirror device (DMD)-based 3D printing of poly(propylene fumarate) scaffolds,
654 Mater. Sci. Eng. C. 61 (2016) 301–311. doi:10.1016/j.msec.2015.11.071.

655 [23] S.D. Gittard, P.R. Miller, C. Jin, T.N. Martin, R.D. Boehm, B.J. Chisholm, S.J. Stafslien,
656 J.W. Daniels, N. Cilz, N.A. Monteiro-Riviere, A. Nasir, R.J. Narayan, Deposition of
657 antimicrobial coatings on microstereolithography-fabricated microneedles, Jom. 63 (2011)
658 59–68. doi:10.1007/s11837-011-0093-3.
659 [24] Y. Lu, S.N. Mantha, D.C. Crowder, S. Chinchilla, K.N. Shah, Y.H. Yun, R.B. Wicker,
660 J.W. Choi, Microstereolithography and characterization of poly(propylene fumarate)-
661 based drug-loaded microneedle arrays, Biofabrication. 7 (2015) 1–13. doi:10.1088/1758-
662 5090/7/4/045001.
663 [25] N. Sreerama, R.W. Woody, Estimation of protein secondary structure from circular
664 dichroism spectra: Comparison of CONTIN, SELCON, and CDSSTR methods with an
665 expanded reference set, Anal. Biochem. 287 (2000) 252–260.
666 doi:10.1006/abio.2000.4880.
667 [26] S.P. Davis, B.J. Landis, Z.H. Adams, M.G. Allen, M.R. Prausnitz, Insertion of
668 microneedles into skin: Measurement and prediction of insertion force and needle fracture
669 force, J. Biomech. 37 (2004) 1155–1163. doi:10.1016/j.jbiomech.2003.12.010.
670 [27] M.J. Uddin, N. Scoutaris, P. Klepetsanis, B. Chowdhry, M.R. Prausnitz, D. Douroumis,
671 Inkjet printing of transdermal microneedles for the delivery of anticancer agents, Int. J.
672 Pharm. 494 (2015) 593–602. doi:10.1016/j.ijpharm.2015.01.038.
673 [28] Z. Yong, D. Yingjie, W. Xueli, X. Jinghua, L. Zhengqiang, Conformational and
674 bioactivity analysis of insulin: Freeze-drying TBA/water co-solvent system in the
675 presence of surfactant and sugar, Int. J. Pharm. 371 (2009) 71–81.
676 doi:10.1016/j.ijpharm.2008.12.018.
677 [29] Y.H. Kim, C. Sioutas, K.S. Shing, Influence of stabilizers on the physicochemical

678 characteristics of inhaled insulin powders produced by supercritical antisolvent process,
679 Pharm. Res. 26 (2009) 61–71. doi:10.1007/s11095-008-9708-y.
680 [30] H. Schiffter, J. Condliffe, S. Vonhoff, Spray-freeze-drying of nanosuspensions: the
681 manufacture of insulin particles for needle-free ballistic powder delivery, J. R. Soc.
682 Interface. 7 (2010) S483-500. doi:10.1098/rsif.2010.0114.focus.
683 [31] L. Whitmore, B.A. Wallace, DICHROWEB, an online server for protein secondary
684 structure analyses from circular dichroism spectroscopic data, Nucleic Acids Res. 32
685 (2004) 668–673. doi:10.1093/nar/gkh371.
686 [32] L. Whitmore, B.A. Wallace, Protein secondary structure analyses from circular dichroism
687 spectroscopy: Methods and reference databases, Biopolymers. 89 (2008) 392–400.
688 doi:10.1002/bip.20853.
689 [33] M.J. Ettinger, S.N. Timasheff, Optical activity of insulin. II. Effect of nonaqueous
690 solvents, Biochemistry. 10 (1971) 831–840.
691 http://www.ncbi.nlm.nih.gov/entrez/query.fcgi?cmd=Retrieve&db=PubMed&dopt=Citati
692 on&list_uids=5544674.
693 [34] B. Sarmento, D.C. Ferreira, L. Jorgensen, M. van de Weert, Probing insulin's secondary
694 structure after entrapment into alginate/chitosan nanoparticles, Eur. J. Pharm. Biopharm.
695 65 (2007) 10–17. doi:10.1016/j.ejpb.2006.09.005.
696 [35] F. Andrade, P. Fonte, M. Oliva, M. Videira, D. Ferreira, B. Sarmento, Solid state
697 formulations composed by amphiphilic polymers for delivery of proteins: characterization
698 and stability, Int. J. Pharm. 486 (2015) 195–206. doi:10.1016/j.ijpharm.2015.03.050.
699 [36] W. Dzwolak, R. Ravindra, J. Lendermann, R. Winter, Aggregation of bovine insulin
700 probed by DSC/PPC calorimetry and FTIR spectroscopy, Biochemistry. 42 (2003) 11347–

11355. doi:10.1021/bi034879h.

[37] J.F. Carpenter, J.H. Crowe, An infrared spectroscopic study of the interactions of carbohydrates with dried proteins, Biochemistry. 28 (1989) 3916–3922. doi:10.1021/bi00435a044.

[38] M.A. Haque, J. Chen, P. Aldred, B. Adhikari, Drying and denaturation characteristics of whey protein isolate in the presence of lactose and trehalose, Food Chem. 177 (2015) 8–16. doi:10.1016/j.foodchem.2014.12.064.

[39] S.G. Melberg, W.C. Johnson, Changes in secondary structure follow the dissociation of human insulin hexamers: A circular dichroism study, Proteins Struct. Funct. Bioinforma. 8 (1990) 280–286. doi:10.1002/prot.340080309.

[40] D.C.O. Nai-Teng Yu, C.S. Liu, Laser Raman Spectroscopy and the Conformation and Proinsulin of Insulin, J. Mol. Biol. 70 (1972) 117–132.

[41] P.O. Souillac, C.R. Middaugh, J.H. Rytting, Investigation of protein / carbohydrate interactions in the dried state . 2 . Diffuse reflectance FTIR studies, Int. J. Pharm. 235 (2002) 207–218.

[42] A. Das, P. Basak, R. Pattanayak, T. Kar, R. Majumder, D. Pal, A. Bhattacharya, M. Bhattacharyya, S.P. Banik, Trehalose induced structural modulation of Bovine Serum Albumin at ambient temperature, Int. J. Biol. Macromol. 105 (2017) 645–655. doi:10.1016/j.ijbiomac.2017.07.074.

[43] J. Lee, S. Timasheff, The Stabilization of Proteins by Sucrose *, J. Biol. Chem. 256 (1981) 7193–7201.

[44] S. Yoshioka, T. Miyazaki, Y. Aso, b-Relaxation of Insulin Molecule in Lyophilized Formulations Containing Trehalose or Dextran As a Determinant of Chemical Reactivity,

Pharm. Res. 23 (2006) 961–966. doi:10.1007/s11095-006-9907-3.

[45] C. Branca, S. MacCarrone, S. Magazu, G. Maisano, S.M. Bennington, J. Taylor, Tetrahedral order in homologous disaccharide-water mixtures, J. Chem. Phys. 122 (2005) 174513-1-174513–6. doi:10.1063/1.1887167.

[46] N.K. Jain, I. Roy, Effect of trehalose on protein structure, Protein Sci. 18 (2009) 24–36. doi:10.1002/pro.3.

[47] G. Zeng, J.J. Shou, K.K. Li, Y.H. Zhang, In-situ confocal Raman observation of structural changes of insulin crystals in sequential dehydration process, Biochim. Biophys. Acta - Proteins Proteomics. 1814 (2011) 1631–1640. doi:10.1016/j.bbapap.2011.09.002.

[48] L.G. Tensmeyer, J.E. Shields, E. Lilly, The Raman Spectra of Crystalline 4Zn, 2Zn, and Na Insulin., 1336 (1990) 222–234.

[49] H. Takeuchi, N. Watanabe, Y. Satoh, I. Harada, Effects of Hydrogen Bonding on the Tyrosine Raman Bands in the 1300-1150 cm - Region, 20 (1989) 233–237.

[50] S.D. Gittard, B. Chen, H. Xu, A. Ovsianikov, B.N. Chichkov, N.A. Monteiro-Riviere, R.J. Narayan, The effects of geometry on skin penetration and failure of polymer microneedles, J. Adhes. Sci. Technol. 27 (2013) 227–243. doi:10.1080/01694243.2012.705101.

[51] I.C. Lee, Y.C. Wu, S.W. Tsai, C.H. Chen, M.H. Wu, Fabrication of two-layer dissolving polyvinylpyrrolidone microneedles with different molecular weights for: In vivo insulin transdermal delivery, RSC Adv. 7 (2017) 5067–5075. doi:10.1039/c6ra27476e.

[52] J. Gupta, S.S. Park, B. Bondy, E.I. Felner, M.R. Prausnitz, Infusion pressure and pain during microneedle injection into skin of human subjects, Biomaterials. 32 (2011) 6823–6831. doi:10.1016/j.biomaterials.2011.05.061.

[53] M. Ling, M. Chen, Dissolving polymer microneedle patches for rapid and efficient transdermal delivery of insulin to diabetic rats., Acta Biomater. 9 (2013) 8952–8961. doi:10.1016/j.actbio.2013.06.029.

[54] S. Liu, M. Jin, Y. Quan, F. Kamiyama, H. Katsumi, T. Sakane, A. Yamamoto, The development and characteristics of novel microneedle arrays fabricated from hyaluronic acid, and their application in the transdermal delivery of insulin., J. Control. Release. 161 (2012) 933–41. doi:10.1016/j.jconrel.2012.05.030.

[55] S. Fakhraei Lahiji, Y. Jang, I. Huh, H. Yang, M. Jang, H. Jung, Exendin-4-encapsulated dissolving microneedle arrays for efficient treatment of type 2 diabetes, Sci. Rep. 8 (2018) 1–9. doi:10.1038/s41598-018-19789-x.

[56] Y. Qiu, G. Qin, S. Zhang, Y. Wu, B. Xu, Y. Gao, Novel lyophilized hydrogel patches for convenient and effective administration of microneedle-mediated insulin delivery, Int. J. Pharm. 437 (2012) 51–56. doi:10.1016/j.ijpharm.2012.07.035.

[57] S.P. Davis, W. Martanto, M.G. Allen, S. Member, M.R. Prausnitz, Hollow Metal Microneedles for Insulin Delivery to Diabetic Rats, 52 (2005) 909–915.